The Astrophysical Journal, 1002:165 (13pp), 2026 May 10 https://doi.org/10.3847/1538-4357/ae5ba0

Magnetic Field Spreading from Stellar and Galactic Dynamos into the Exterior

Axel Brandenburg[1,2,3,4], Oindrila Ghosh[5], Franco Vazza[6,7], and Andrii Neronov[8,9]
[1] Nordita, KTH Royal Institute of Technology and Stockholm University, Hannes Alfvéns väg 12, SE-10691 Stockholm, Sweden
[2] The Oskar Klein Centre, Department of Astronomy, Stockholm University, AlbaNova, SE-10691 Stockholm, Sweden
[3] McWilliams Center for Cosmology & Department of Physics, Carnegie Mellon University, Pittsburgh, PA 15213, USA
[4] School of Natural Sciences and Medicine, Ilia State University, 3-5 Cholokashvili Avenue, 0194 Tbilisi, Georgia
[5] Oskar Klein Centre for Cosmoparticle Physics, Department of Physics, Stockholm University, AlbaNova, 10691 Stockholm, Sweden
[6] Dipartimento di Fisica e Astronomia, Universita di Bologna, Via Gobetti 93/2, 40129 Bologna, Italy
[7] INAF Istituto di Radioastronomia, Via P. Gobetti 101, 40129 Bologna, Italy
[8] Université Paris Cité, CNRS, Astroparticule et Cosmologie, 75006 Paris, France
[9] Laboratory of Astrophysics, École Polytechnique Fédérale de Lausanne, 1015 Lausanne, Switzerland
Received 2025 December 23; revised 2026 March 18; accepted 2026 April 3; published 2026 May 5

Abstract

The exteriors of stellar and galactic dynamos are usually modeled as current-free potential fields. A more realistic description might instead be that of a force-free magnetic field. Here, we suggest that, in the absence of outflows, neither of these reflects the actual behavior when the magnetic field spreads diffusively into a more poorly conducting turbulent exterior outside dynamo. In particular, we explain why the usual ordering, in which the dipole magnetic field is the most slowly decaying one, is altered, and why the quadrupole can develop a toroidal component that decays even more slowly with radial distance. This is a robust feature that persists even for spatially nonuniform magnetic diffusivities. It is most clearly seen for spherical dynamo volumes and becomes more complicated for oblate ones. In either case, however, these fields are confined within a magnetosphere, beyond which the field strength drops exponentially. We demonstrate that the Faraday displacement current, which plays a role in a vacuum, can safely be neglected in all cases. The superposition of magnetic fields from galaxies in the outskirts of voids between galaxy clusters therefore cannot explain the magnetization of the intergalactic medium in voids, reinforcing the conventional expectation that these fields are of primordial origin. For quadrupolar configurations, the synchrotron emission from the magnetosphere is found to be constant along concentric rings. The dipolar and quadrupolar configurations display large-scale radial trends that are potentially distinguishable with existing radio telescopes.

Unified Astronomy Thesaurus concepts: Cosmic magnetic fields theory (321)

1. Introduction

The magnetic fields in stars and galaxies can be explained by dynamo action, which converts the kinetic energy of turbulence and differential rotation into magnetic energy. Such systems are traditionally computed by assuming that the magnetic field outside the dynamo domain continues as a current-free potential field. Mathematically, this can be formulated as a suitable boundary condition applied at the outer radius of a spherical (M. Steenbeck & F. Krause 1969) or ellipsoidal domain (M. Stix 1975). In cylindrical and several other coordinate systems, however, no method exists to apply a potential-field boundary condition. One possibility is then to adopt a perfectly conducting boundary condition (R. Meinel et al. 1990). However, a more physical approach may be to embed the galaxy in a poorly conducting exterior (A. Brandenburg et al. 1990; D. Elstner et al. 1990), as this would approximate a vacuum in the limit of zero conductivity.

The assumption of a vacuum outside the dynamo has never been thought to be more than a mathematically convenient construct. However, in recent work by D. Garg et al. (2025), a vacuum was assumed to exist even in the far field of galaxies. Their study, which does not include outflows or winds of any type, led to subsequent investigations addressing the nature of the magnetic field in the far field of galaxies (K. Seller & G. Sigl 2025; O. Ghosh et al. 2026). The present paper follows up on our earlier work (O. Ghosh et al. 2026). Here, we focus on a more detailed numerical study, approach in some cases the limit of extremely poor conductivity, and relate our results with potential observations of synchrotron emission.

It is commonly assumed that a more realistic boundary condition for a dynamo corresponds to an electrically conducting exterior, though not necessarily a perfectly conducting one. In addition, if the exterior has low density and is at rest, the magnetic field would be force-free, i.e., the cross product of current density and magnetic field vanishes. In MHD, where the current density is proportional to the curl of the magnetic field, this implies that the two fields are parallel. Such fields are therefore eigenfunctions of the curl operator and are known as Chandrasekhar–Kendall functions (after the early paper by S. Chandrasekhar & P. C. Kendall 1957). In the context of plasma confinement configurations, force-free magnetic fields are likewise often more realistic than the assumption of a vacuum (J. P. Freidberg 2014).

Adopting a perfectly force-free magnetic field is generally problematic, because such configurations may not be topologically realizable and would take significant time to establish in the vast exterior of a dynamo. To alleviate this problem, a commonly used approach in solar physics is the magneto-frictional method (W. H. Yang et al. 1986), in which the Lorentz force drives flows through a friction term. These flows relax the field until the force is minimized. In a similar

approach, we study here the spreading of galactic magnetic fields into intergalactic space by solving the mean-field momentum equation and modeling the dynamo exterior as a medium with a certain viscosity and electrical conductivity. A vacuum corresponds to the limit of very low conductivity, or equivalently very high magnetic diffusivity. A large effective magnetic diffusivity can emerge in a turbulent environment when modeling the large-scale field as an average or mean field, $\overline{\boldsymbol{B}}$, where the overbar denotes an appropriate averaging procedure. However, as we explain below, the diffusivity needed to reproduce the electrical properties of a vacuum would be at least 8 orders of magnitude larger than can reasonably be explained by turbulence.

It is useful to represent the resulting magnetic field as a multipole expansion with terms proportional to spherical harmonics $Y_\ell^m(\theta, \phi)$, where ℓ and m are the spherical harmonic degree and order, respectively. For a vacuum, the magnetic field decays with radius r as $r^{-(\ell+2)}$. The lowest multiple is the dipole with $\ell = 1$, for which the field decays as r^{-3}, while for a quadrupole, $\ell = 2$, it decays as r^{-4}. In an electrically conducting environment, magnetic fields are expected to be close to force-free and can therefore decay differently. If the gas pressure is negligible, force-free magnetic fields obey $\overline{\boldsymbol{J}} \times \overline{\boldsymbol{B}} = 0$, i.e., the current density $\overline{\boldsymbol{J}} = \boldsymbol{\nabla} \times \overline{\boldsymbol{B}}/\mu_0$, with μ_0 being the vacuum permeability, is parallel to $\overline{\boldsymbol{B}}$. This means that $\boldsymbol{\nabla} \times \overline{\boldsymbol{B}} = \alpha_{\rm ff} \overline{\boldsymbol{B}}$, where $\alpha_{\rm ff}$ is a coefficient that is constant along magnetic field lines but may vary perpendicular to them (E. R. Priest 1982).

To explain the toroidal magnetic fields observed around solar-type stars, A. Bonanno (2016) and A. Bonanno & F. Del Sordo (2017) considered force-free magnetic fields in mean-field dynamo exteriors. They assumed the coronal magnetic field of those stars to be harmonic, but did not address how such configurations can be achieved on finite timescales. Here, we show that such fields can only be produced within a finite but slowly expanding magnetosphere around the dynamo. This also has implications for galactic dynamos and for the question of whether such configurations can explain the magnetic fields in the voids between galaxy clusters (D. Garg et al. 2025; K. Seller & G. Sigl 2025; O. Ghosh et al. 2026).

O. Ghosh et al. (2026) showed that the growth of the magnetosphere changes from ballistic to diffusive once the dynamo saturates. They also demonstrated that a quadrupolar magnetic field in the magnetosphere decays with radius r only as r^{-2}, which is slower than the r^{-3} decay of a dipolar field—both in a vacuum and in a conducting exterior. Here, we present a detailed analysis of these empirical findings and elucidate the origin of the slow radial decay for quadrupolar fields. In particular, we explore the vacuum limit considered by D. Garg et al. (2025), and compute the resulting synchrotron emission from our quadrupolar field.

In Section 2, we present the details of our model, allowing for different profiles of the effective magnetic diffusivity, as well as feedback from mean flows and, in some cases, the effects of a finite speed of light. Our results on the establishment of a time-dependent magnetosphere are presented in Section 3. In Section 4, we discuss new observational constraints in terms of synchrotron radio emission, which go beyond the rotation measure diagnostics presented in O. Ghosh et al. (2026). Finally, we conclude in Section 5.

2. Our Model

2.1. Basic Equations

We solve the mean-field dynamo equations using spherical coordinates, (r, θ, ϕ). Before making the MHD approximation, in which the Faraday displacement current is omitted, we begin with the full set of Maxwell equations, which are also applicable to an extremely poorly conducting medium or to the vacuum considered by D. Garg et al. (2025). To quantify the difference between a poorly conducting exterior and a vacuum, we also include in some cases the Faraday displacement current. The detailed motivation for this approach, along with first results, was presented by O. Ghosh et al. (2026).

The displacement current can become important when the ordinary current density is small. We assume that the mean current density $\overline{\boldsymbol{J}}$ obeys Ohm's law, which in our case takes the form

$$\overline{\boldsymbol{J}} = \sigma(\overline{\boldsymbol{E}} + \overline{\boldsymbol{U}} \times \overline{\boldsymbol{B}} + \overline{\boldsymbol{u} \times \boldsymbol{b}}), \tag{1}$$

where σ is the microphysical conductivity, $\overline{\boldsymbol{E}}$ is the mean electric field, $\overline{\boldsymbol{U}}$ is the mean velocity, $\overline{\boldsymbol{B}}$ is the mean magnetic field, and $\overline{\boldsymbol{u} \times \boldsymbol{b}}$ is the mean electromotive force resulting from the small-scale velocity and magnetic fields, $\boldsymbol{u}$ and $\boldsymbol{b}$, respectively. In its simplest form, the mean electromotive force can be written as

$$\overline{\boldsymbol{u} \times \boldsymbol{b}} = \alpha \overline{\boldsymbol{B}} - \eta_{\rm turb}\, \mu_0 \overline{\boldsymbol{J}}, \tag{2}$$

where α is a coefficient that emerges in the calculation of $\overline{\boldsymbol{u} \times \boldsymbol{b}}$ for helical turbulence (H. K. Moffatt 1978). It can lead to the growth and sustenance of a mean magnetic field and is generally referred to as the α-effect. Furthermore, the quantity $\eta_{\rm turb}$ denotes the turbulent magnetic diffusivity.

It is convenient to define the microphysical magnetic diffusivity $\eta = (\mu_0 \sigma)^{-1}$ along with the total (effective) magnetic diffusivity $\eta_{\rm eff} = \eta + \eta_{\rm turb}$. Ohm's law for the mean current density can then be written as

$$\mu_0 \overline{\boldsymbol{J}} = (\overline{\boldsymbol{E}} + \overline{\boldsymbol{U}} \times \overline{\boldsymbol{B}} + \alpha \overline{\boldsymbol{B}})/\eta_{\rm eff}. \tag{3}$$

The term $\mu_0 \overline{\boldsymbol{J}}$ appears as the second term on the right-hand side (rhs) of the averaged Ampère–Maxwell equation:

$$\frac{1}{c^2} \frac{\partial \overline{\boldsymbol{E}}}{\partial t} = \boldsymbol{\nabla} \times \overline{\boldsymbol{B}} - \mu_0 \overline{\boldsymbol{J}}, \tag{4}$$

where c is the speed of light.

The full set of Maxwell equations can then be written as

$$\frac{\partial \overline{\boldsymbol{A}}}{\partial t} = -\overline{\boldsymbol{E}}, \qquad \overline{\boldsymbol{B}} = \boldsymbol{\nabla} \times \overline{\boldsymbol{A}}, \tag{5}$$

along with

$$-\left(1 + \frac{\eta_{\rm eff}}{c^2} \frac{\partial}{\partial t}\right) \overline{\boldsymbol{E}} = \overline{\boldsymbol{U}} \times \overline{\boldsymbol{B}} + \alpha \overline{\boldsymbol{B}} - \eta_{\rm eff}\, \boldsymbol{\nabla} \times \overline{\boldsymbol{B}}, \tag{6}$$

where $\overline{\boldsymbol{A}}$ is the mean magnetic vector potential, so that the mean magnetic field is given by $\overline{\boldsymbol{B}} = \boldsymbol{\nabla} \times \overline{\boldsymbol{A}}$, which satisfies the constraint $\boldsymbol{\nabla} \cdot \overline{\boldsymbol{B}} = 0$. The mean charge density is given by $\overline{\rho}_{\rm e} = \epsilon_0\, \boldsymbol{\nabla} \cdot \overline{\boldsymbol{E}}$, where $\epsilon_0 = 1/\mu_0 c^2$ is the vacuum permittivity. Here, we have adopted the Weyl gauge, i.e., the electrostatic potential vanishes.

The Faraday displacement current, $\epsilon_0 \partial \overline{\boldsymbol{E}}/\partial t$, can be neglected when $\eta_{\rm eff} \ll \tau c^2$, where τ is a characteristic

timescale. In this limit, the MHD approximation applies and the terms on the rhs of Equation (6) can be directly inserted into the rhs of Equation (5), yielding the familiar induction equation. We refer to Appendix A for a discussion of the dispersion relation of a dynamo with an α-effect and a finite value of c, for the simple Cartesian case in a periodic domain with constant coefficients and no feedback from mean gas motions, i.e., $\overline{\boldsymbol{U}}=0$. There, and throughout the main paper, we identify τ with the light travel time, i.e., with $(ck)^{-1}$ or R/c, where k is the wavenumber of the lowest dynamo mode in a periodic domain, and R is the radius of the dynamo in an open domain. Thus, we have $\eta_{\rm eff}\ll c/k$ and $\eta_{\rm eff}\ll cR$ in these two cases.

It is important to stress that the nature of the basic equations changes from parabolic to hyperbolic when the displacement current is included. This also implies that the computational time-step constraint changes from being quadratic to linear in the mesh spacing, which can significantly alleviate the computational restrictions of explicit schemes.

To account for the mean gas motions driven by the magnetic field, we also solve in some cases the momentum equation, assuming an isothermal gas. The sound speed $c_{\rm s}$ is then constant, and the mean pressure $\overline{p}(x,z,t)$ is given by $\overline{p}=\overline{\rho}c_{\rm s}^2$. Mean-field hydromagnetic equations of this type have been studied by many authors, starting with the work by M. Schüssler (1979) in Cartesian geometry, and subsequently A. Brandenburg et al. (1992), L. L. Kitchatinov & G. Rüdiger (1995), and M. Rempel (2006). The full system of equations is then complemented by those for $\overline{\rho}$ and $\overline{\boldsymbol{U}}$, i.e.,

$$\frac{D\ln\bar{\rho}}{Dt}=-\boldsymbol{\nabla}\cdot\bar{\boldsymbol{U}}, \tag{7}$$

$$\frac{D\bar{\boldsymbol{U}}}{Dt}=-c_{\rm s}^2\boldsymbol{\nabla}\ln\bar{\rho}+[\bar{\boldsymbol{J}}\times\bar{\boldsymbol{B}}+\boldsymbol{\nabla}\cdot(2\nu_{\rm eff}\bar{\rho}\bar{\mathsf{S}})]/\bar{\rho}, \tag{8}$$

where $D/Dt=\partial/\partial t+\bar{\boldsymbol{U}}\cdot\boldsymbol{\nabla}$ is the advective derivative, and $\overline{\mathsf{S}}$ is the rate-of-strain tensor of the mean flow, with components $\overline{\mathsf{S}}_{ij}=(\overline{U}_{i;j}+\overline{U}_{j;i})/2-\delta_{ij}\boldsymbol{\nabla}\cdot\overline{\boldsymbol{U}}/3$. Here, semicolons denote covariant derivatives.

There are three mean-field parameters: the α-effect, the turbulent (effective) viscosity $\nu_{\rm eff}$, and the turbulent (effective) magnetic diffusivity $\eta_{\rm eff}$. In addition to the macrophysical backreaction from the mean Lorentz force $\overline{\boldsymbol{J}}\times\overline{\boldsymbol{B}}$, we also allow for microphysical feedback in the form of α-quenching (T. S. Ivanova & A. A. Ruzmaikin 1977), and assume α to be proportional to a quenching factor,

$$Q(\overline{\boldsymbol{B}})=1/(1+\overline{\boldsymbol{B}}^2/B_{\rm eq}^2), \tag{9}$$

where $B_{\rm eq}$ is the equipartition field strength above which α begins to be affected by the Lorentz-force feedback from the small-scale magnetic field.

2.2. Details of the Model

In the following, we adopt the computational domain $r_{\rm in}\leqslant r\leqslant r_{\rm out}$ and $0\leqslant\theta\leqslant\pi/2$, and assume axisymmetry, i.e., $\partial/\partial\phi=0$. In Equation (3), we must specify spatial profiles for α and ηT. To model a localized dynamo-active region, we choose α to be finite around the origin and zero outside the dynamo region.

We mostly study spherical dynamo regions with a given radius R, but in some cases we also allow the region to be oblate. In those cases, the disk thickness in the z-direction, i.e., along the axis, is denoted by h. To model a smooth transition, we adopt an error-function profile. In addition, α should be antisymmetric about $z=0$, which is accomplished by multiplying by an additional factor z/h. Thus, we write the α-effect in the form

$$\alpha=\alpha_0\frac{z}{h}\frac{Q(\overline{\boldsymbol{B}})}{2}\left[1-\mathrm{erf}\frac{\sqrt{(\varpi/R)^2+(z/h)^2}-1}{w/R}\right], \tag{10}$$

where α_0 is a constant, $\varpi=r\sin\theta$ is the cylindrical radius, $z=r\cos\theta$ is the height above the midplane, and w is the width of the transition from the dynamo-active region to the exterior. For $h=R$, the dynamo region is spherical.

For $\eta_{\rm eff}$, we allow the effective magnetic diffusivity to take a larger $\eta_{\rm eff}^{\rm ext}$ value outside the dynamo region and to equal $\eta_{\rm eff}^{\rm int}\leqslant\eta_{\rm eff}^{\rm ext}$ within it. We construct the profile for $\eta_{\rm eff}$ in a manner similar to that of α, except that it is symmetric about $z=0$ and does not include a quenching factor. Thus, we choose the profile for $\eta_{\rm eff}$ to be given by

$$\eta_{\rm eff}=\eta_{\rm eff}^{\rm int}+\frac{\eta_{\rm eff}^{\rm ext}-\eta_{\rm eff}^{\rm int}}{2}\left[1+\mathrm{erf}\frac{\sqrt{(\varpi/R)^2+(z/h)^2}-1}{w/R}\right]. \tag{11}$$

We also study some models in which $\eta_{\rm eff}$ is uniform throughout the domain, i.e., $\eta_{\rm eff}^{\rm ext}=\eta_{\rm eff}^{\rm int}$, as well as models in which $\eta_{\rm eff}$ increases gradually in the exterior following a power law. In those cases, we take

$$\eta_{\rm eff}^{\rm ext}=\eta_{\rm eff}^{\rm int}(1+r/r_0)^m, \tag{12}$$

where $m>0$ is the exponent and r_0 is a parameter that determines how rapidly $\eta_{\rm eff}$ increases in the exterior.

To avoid the coordinate singularity at $r=0$, we assume a finite value of $r_{\rm in}=0.1\,R$ in most cases. For the outer radius, we assume $r_{\rm out}=1000\,R$. We restrict ourselves to solving the equations in the first quadrant of the meridional plane, i.e., $0\leqslant\theta\leqslant\pi/2$. This means that, for dipolar fields, $\overline{B}_\theta$ is finite at the equator, while $\overline{B}_r$ and $\overline{B}_\phi$ are vanishing. For quadrupolar fields, by contrast, $\overline{B}_r$ and $\overline{B}_\phi$ are finite at equator, while $\overline{B}_\theta$ is vanishing. In terms of the components of $\overline{\boldsymbol{A}}$, we thus impose the following boundary conditions on $\theta=\pi/2$ (S. Jabbari et al. 2015):

$$\frac{\partial\overline{A}_r}{\partial\theta}=\overline{A}_\theta=\frac{\partial\overline{A}_\phi}{\partial\theta}=0 \tag{13}$$

for dipolar (odd-parity) fields, and

$$\overline{A}_r=\frac{\partial\overline{A}_\theta}{\partial\theta}=\overline{A}_\phi=0 \tag{14}$$

for quadrupolar (even-parity) fields. In the radial direction, we impose a perfect-conductor boundary condition at both ends, i.e., $\overline{A}_\theta=\overline{A}_\phi=0$. Owing to the use of the Weyl gauge, analogous boundary conditions in both directions also apply to the components of $\overline{\boldsymbol{E}}$.

In all our models, we use as an initial condition weak, Gaussian-distributed noise for $\overline{\boldsymbol{A}}$. This acts as a seed magnetic field required for the dynamo to amplify the field exponentially once α_0 is large enough. Owing to the $Q(\overline{\boldsymbol{B}})$ factor, the growth becomes quenched and $|\overline{\boldsymbol{B}}|$ reaches values close to $B_{\rm eq}$. The initial values of $\overline{\boldsymbol{E}}$ and $\overline{\boldsymbol{U}}$ are set to zero, and $\overline{\rho}$ is set to a

constant reference value ρ_0. We recall that gravity is not included in our models.

The strength of the α-effect is quantified by the dynamo number $C_\alpha = \alpha_0 R/\eta_{\rm eff}^{\rm int}$. The diffusivity contrast is given by $C_\eta = \eta_{\rm eff}^{\rm ext}/\eta_{\rm eff}^{\rm int}$. Time is often expressed in terms of the diffusion time $\tau_{\rm diff} = R^2/\eta_{\rm eff}^{\rm ext}$ based on the exterior diffusivity. During the kinematic growth phase, the growth rate γ of the magnetic field is characterized by the nondimensional number $C_\gamma = \gamma R^2/\eta_{\rm eff}^{\rm int}$. Unlike C_α and C_η, which are input parameters, C_γ is an output parameter.

For all spherical simulations, we use a mesh of 8192×32 points in $r_{\rm in} \leqslant r \leqslant 1000\,R$ and $0 \leqslant \theta \leqslant \pi/2$. We use the PENCIL CODE (Pencil Code Collaboration et al. 2021), where the inclusion of the displacement current is facilitated by the `special/disp_current.f90` module, and its mean-field implementation through the `magnetic/meanfield.f90` module. This implementation has been validated by reproducing $\gamma(k)$ from the dispersion relation for constant coefficients in the Cartesian case; see Appendix A. For earlier work with the PENCIL CODE in spherical geometry, where the mean-field momentum equation was included, we refer to S. Jabbari et al. (2015) and P. Jakab & A. Brandenburg (2021). In both studies, gravity played an important role; however, in the present case it could lead to the development of a Parker wind, which we want to suppress. Therefore, we set the gravitational potential to zero.

As an empirical measure of the front speed in simulations including the displacement current, we determine the radius $r_{0.01}$, where the compensated latitudinally averaged magnetic field has dropped to 0.01 times the value inside the magnetosphere. We expect that $r_{0.01}/ct < 1$ in all cases, which is indeed borne out by the simulations.

As already discussed in O. Ghosh et al. (2026), the front speed is constant during the kinematic growth phase. We refer to this growth as ballistic. In the saturated state, the front speed decreases as the radius grows diffusively. Thus, for the front radius $r_*(t)$, we have

$$r_*^2(t) = \begin{cases} q_{\rm ballistic}\,\gamma\eta_{\rm eff}^{\rm ext}\,(t-t_*)^2 & \text{(kinematic phase)},\\ q_{\rm diff}\,\eta_{\rm eff}^{\rm ext}\,(t-t_*) & \text{(saturated phase)}, \end{cases} \tag{15}$$

where $q_{\rm ballistic}$ and $q_{\rm diff}$ are empirical coefficients of order unity, and t_* denotes the time at which the corresponding growth behavior becomes fully established.

2.3. Application to Galactic Scales

In this work, we present our results in dimensionless form by expressing length in units of R and time in units of $\tau_{\rm diff} \equiv R^2/\eta_{\rm eff}^{\rm ext}$. In a specific example, O. Ghosh et al. (2026) estimated $\eta_{\rm eff}^{\rm ext} = 3000$ kpc km s^{-1}. They presented their results in dimensional form. The corresponding dimensionless time at the end of their runs, $t_{\rm end}/\tau_{\rm diff}$, was about 1400. Identifying $t_{\rm end}$ with the Hubble time of 14 Gyr yields $\tau_{\rm diff} = 0.01$ Gyr. The length unit is therefore $R = (\eta_{\rm eff}^{\rm ext}\tau_{\rm diff})^{1/2} \approx 5.5$ kpc. For one Hubble time, O. Ghosh et al. (2026) quoted a typical diffusion length of 200 kpc; see their Table II for a case they refer to as "cosmic web dynamics."

We reiterate that our intention is not to provide a realistic model of a galactic dynamo. Instead, we aim to understand the far-field behavior of a generic dynamo. Our results may therefore in principle also be applicable to stellar dynamos. We stress that differential rotation is not included either. All these simplifications are made to keep the system sufficiently transparent to identify potentially generic behaviors expected in the far field of astrophysical dynamos in general.

3. Results

3.1. Exponential Growth Phase

Let us first look at the initial spreading of a dynamo-generated magnetic field into the region $r > R$. We adopt an α-effect in the range $r_{\rm in} \leqslant r \leqslant R$ with $C_\alpha = 25$, and assume a 10- or 50-fold increase of $\eta_{\rm eff}$ in the exterior; see Table 1 for a summary of the runs discussed in this paper. The three runs of O. Ghosh et al. (2026) are included in Table 1 as Runs A–C.

At early times, the magnetic field expands into $r > R$ and is found to fall off with distance as $e^{-\kappa r}$, where

$$\kappa = (\gamma/\eta_{\rm turb})^{1/2} \tag{16}$$

is the radial decay rate, γ is the growth rate, and ηt is the turbulent magnetic diffusivity. This scaling is analogous to that for the skin effect, except that here we use an imaginary frequency, which leads to a nonoscillatory decay with increasing distance from the dynamo regime.

Since the magnetic field still increases exponentially as $e^{\gamma t}$, we have $B \sim e^{-\kappa r+\gamma t} = e^{-\kappa(r-c_{\rm front}t)}$, where $c_{\rm front} = \gamma/\kappa = (\gamma\eta_{\rm turb})^{1/2}$ is the front speed, as obtained from Equation (16). After an initial transient phase, the front radius begins to increase linearly with time; see Figure 1. This scaling is similar to that describing the propagation of fronts in epidemiological models (J. D. Murray et al. 1986). It also applies to the turbulent propagation of reactive fronts in combustion when the reaction speed exceeds the diffusion speed (A. Brandenburg et al. 2011).

3.2. Magnetosphere Radius

In Figure 2, we plot the latitudinally averaged rms magnetic field for dipolar and quadrupolar boundary conditions. For the quadrupolar case, we also include a model with a fivefold smaller magnetic diffusivity in the exterior. These three models were also discussed in O. Ghosh et al. (2026). It turns out that, during the early kinematic growth phase, the magnetic field grows and spreads in a similar manner, regardless of its hemispheric parity and the value of the exterior magnetic diffusivity. After the magnetic field has saturated in the dynamo-active region, it continues to spread as r^{-3} in the dipolar case, but as r^{-2} in the two quadrupolar cases. This behavior can clearly be seen in Figure 2. Note also that, during the kinematic phase, the field decays more rapidly with radius than in the saturated phase. Indeed, this represents a transient phase in which the magnetic field transitions from an exponential radial decay, $\propto e^{-\kappa r}$, to a power-law decay, $\propto r^{-n}$, within a shell around the dynamo, which subsequently becomes the magnetosphere.

The radial power-law decay extends from the end of the dynamo-active region at $r = R$ to a radius $r_*(t)$, which we defined as the front radius in Equation (15). This radius grows diffusively with time after a reference time t_*. As already demonstrated by O. Ghosh et al. (2026), the sphere of radius $r_*(t)$ can be interpreted as a magnetosphere. For the nondimensional coefficient $q_{\rm diff}$ in Equation (15), the empirically determined value is close to 2—analogous to the law of

Table 1
Summary of Runs Presented in This Paper

Run	sym	$\overline{U}$	$cR/\eta_{\rm eff}$	$r_{\rm in}/R$	h/R	m	C_α	C_η	C_γ	$B_0/B_{\rm eq}$	$q_{\rm diff}$[a]	$r_{0.01}/ct$[b]	n
A	D	$\neq 0$	∞	0.1	1	0	25	50	63	0.7	4.9	⋯	3
B	Q	$\neq 0$	∞	0.1	1	0	25	50	66	0.4	2.5	⋯	2
C	Q	$\neq 0$	∞	0.1	1	0	25	10	70	0.4	2.5	⋯	2
D	D	0	∞	0.1	1	0	25	1	74	0.7	4.9	⋯	3
E	D	0	1	0.1	1	0	25	1	7.2	0.7	⋯	0.8	3
F	D	0	0.5	0.1	1	0	25	1	3.7	0.7	⋯	0.6	3
G	Q	0	∞	0.1	1	0	25	1	77	0.4	2.5	⋯	2
G′	Q	0	∞	0.1	1	1	25	r^{-m}	68	0.4	2.5	⋯	2.16
G″	Q	0	∞	0.1	1	1.5	25	r^{-m}	68	0.4	2.5	⋯	2.23
H	Q	0	1	0.1	1	0	25	1	8.2	0.4	⋯	0.7	2
I	Q	0	0.5	0.1	1	0	25	1	4.2	0.4	⋯	0.6	2
J	Q	0	∞	0.2	1	0	50	1	386	0.6	2.5	⋯	2
K	Q	0	∞	0.1	0.5	0	50	1	348	0.2	2.5	⋯	2
L	Q	0	∞	0.1	0.2	0	50	1	78	2×10^{-5}	2.5	⋯	2

Notes.
[a] A hyphen indicates that Equation (17) does not provide an appropriate fit.
[b] The ratio $r_{0.01}/ct$ can only be evaluated when c is finite.

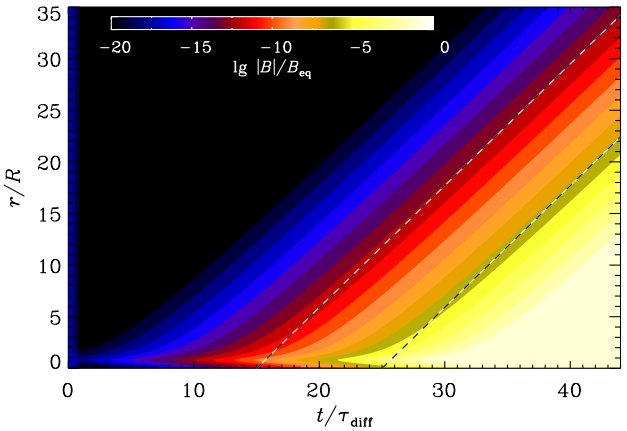

Figure 1. Color-scale representation of $\ln|\boldsymbol{B}|$ vs. r and t for Run B. Yellow (blue) shades denote large (small) field strengths. The dynamo operates in $0 \leqslant r \leqslant 1$, as can be seen by the elevated field strength close to $r = 0$. The left (right) dashed line corresponds to $q_{\rm ballistic} = 1$ with $t_*/\tau = 15$ (25).

Brownian diffusion (A. Einstein 1905). In Figure 2, we also compare the modulus of the latitudinally averaged magnetic field at the final time step with a fit of the form

$$\overline{B}(r,\,t) = B_0 \left(\frac{r}{1\ {\rm kpc}}\right)^{-n} \exp\{-\frac{1}{2}[r/r_*(t)]^2\}, \qquad (17)$$

where B_0 characterizes the magnetic field strength inside the magnetosphere and n is the radial decay exponent. We find that the value of $q_{\rm diff}$ is around 4.9 for dipolar configurations and around 2.5 for quadrupolar configurations; see Table 1. This demonstrates that the radius of the magnetosphere scales with the exterior magnetic diffusivity, $\eta_{\rm turb}^{\rm ext}$, and is also independent of the diffusivity contrast, C_η. Even the case $C_\eta = 1$ results in the same scaling expected for the value $\eta_{\rm turb}^{\rm ext}$, which is then also equal to $\eta_{\rm turb}^{\rm ext}$ in that case.

Following O. Ghosh et al. (2026), we determine the instantaneous front radius $r_*(t)$ as a weighted integral:

$$r_*(t) = \int r^{n+1}\overline{B}(r,\,t)\,dr \Big/ \int r^n \overline{B}(r,\,t)\,dr. \qquad (18)$$

The diffusive $r_*(t) \propto t^{1/2}$ scaling is confirmed for all runs where $\eta_{\rm eff} = {\rm const} = \eta_{\rm turb}^{\rm ext}$ in the exterior; see Run D (similar to Run A) and Run J (similar to Run B). The similarity between these pairs of runs also shows that neither the value of C_η nor the inclusion of feedback from the mean flow has a noticeable effect. Since the latter would act in a manner analogous to the aforementioned magneto-frictional approach, we conclude that the magnetic fields are already close to being force-free.

3.3. Radially Varying Diffusivity

The local front speed depends on the value of $\eta_{\rm eff}$. When this is a function of r, the front speed can increase in regions where $\eta_{\rm eff}$ is larger. Thus, for a radially increasing profile, i.e., $m > 0$ in Equation (12), we expect the front speed to increase with r. This behavior is demonstrated in Figure 3, where we compare $r_*(t)$ for Runs G′ and G″ with $m = 1$ and 1.5 to the case $m = 0$. Here, we adopt $r_0/R = 10$ in Equation (12). At large radii, we find a steeper temporal growth, with $\propto t^{0.8}$ for $m = 1$ and $\propto t^{1.3}$ for $m = 1.5$. However, the shallow inverse-quadratic radial decay of the mean magnetic field for the quadrupolar case remains approximately valid. In Appendix B, we demonstrate that more precise measurements yield slightly steeper radial decays, with $n \approx 2.16$ and 2.23 for models with $m = 1$ and 1.5, respectively.

The temporal scalings of $r_*(t)$ for different values of m give an approximate idea about the sensitivity. We see that the lines remain still somewhat curved, indicating the absence of a true power-law scaling. If the turbulent magnetic diffusivity outside the galaxy were highly variable, we might expect a corrugated magnetosphere. Conversely, if the magnetosphere is not strongly corrugated, this would suggest a more uniform distribution of r_*. In either case, however, the spatial scaling of the magnetic field within the magnetosphere remains approximately $\propto r^{-2}$ for the quadrupolar configuration.

3.4. Comments on Nonuniform Diffusive Scalings

It is tempting to refer to diffusive scaling as one that scales as $t^{1/2}$ with time. Conversely, one might refer to deviations from this behavior as nondiffusive. This is,

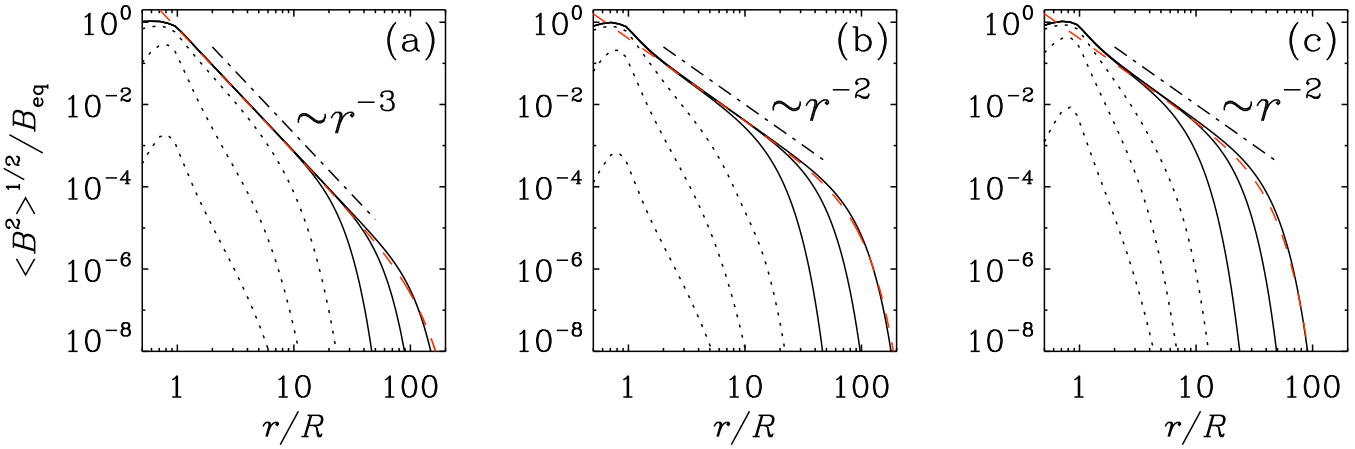

Figure 2. Radial dependence of $\langle \boldsymbol{B}^2\rangle^{1/2}$ at times $t/\tau_{\rm diff} = 30$, 35, and 50 (dotted lines), and $t/\tau_{\rm diff} = 100$, 300, and 1000 (solid lines), for (a) a dipolar field with $C_\eta = 50$ (Run A), (b) a quadrupolar field with $C_\eta = 50$ (Run B), and (c) a quadrupolar field with $C_\eta = 10$ (Run C). The asymptotic falloffs $\propto r^{-3}$ for the dipolar field and $\propto r^{-2}$ for the quadrupolar fields are marked with dashed–dotted lines. The red lines denote fits given by Equation (17), using the $q_{\rm diff}$ values listed in Table 1.

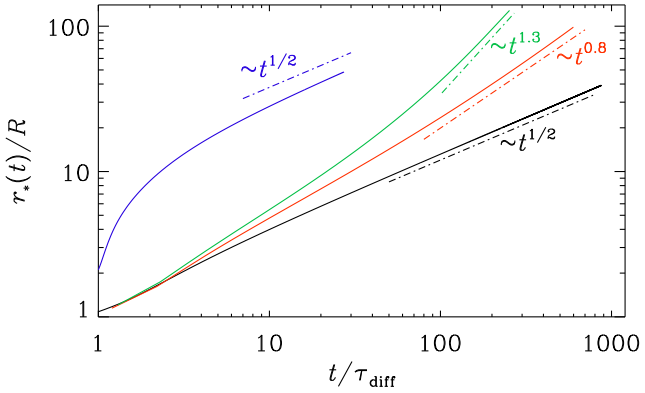

Figure 3. Comparison of $r_*(t)$ for Runs B (blue), G (black), G′ (red), and G″ (green).

however, misleading, because the expansion speed remains limited by the local magnetic diffusivity. We can see this by inserting Equation (12) into Equation (15) for the saturated phase, and assuming $r \gg r_0$, which yields

$$r_*(t)/r_0 \approx [q_{\rm diff}\, \eta_{\rm eff}^{\rm ext}\, (t - t_*)/r_0^2]^{1/(2-m)}. \tag{19}$$

Thus, if correct, we might asymptotically expect a temporal growth $\propto t$ for $m = 1$ (instead of the numerically obtained $t^{0.8}$ behavior) and $\propto t^2$ for $m = 1.5$ (instead of $t^{1.3}$). This discrepancy is consistent with the fact that the lines in Figure 3 remain somewhat curved, indicating that a true power-law scaling has not yet been reached.

We emphasize that the accelerated expansion does not affect our conclusion that magnetic fields cannot significantly extend into cosmic voids. This would require unrealistically large levels of turbulence in the voids. We return to this point later in the paper when making a more quantitative comparison with the vacuum case.

3.5. Radial Power-law Scaling within the Magnetosphere

To study the radial power-law behavior for dipolar and quadrupolar configurations in more detail, we now express the latitudinal dependence in terms of Legendre polynomials. An axisymmetric magnetic field can be written as (H. K. Moffatt 1978; E. N. Parker 1979; F. Krause & K.-H. Rädler 1980)

$$\overline{\boldsymbol{B}} = \hat{\boldsymbol{\phi}}\overline{B}_\phi + \boldsymbol{\nabla}\times\hat{\boldsymbol{\phi}}\overline{A}_\phi, \tag{20}$$

where $\overline{A}_\phi(r,\,\theta,\,t)$ and $\overline{B}_\phi(r,\,\theta,\,t)$ are independent of each other outside the dynamo region and characterize the poloidal and toroidal magnetic field decay in the radial direction. These functions can be expanded as[10]

$$\overline{A}_\phi = \sum a_\ell(r)\, P_\ell^1(\cos\theta), \quad \overline{B}_\phi = \sum b_\ell(r)\, P_\ell^1(\cos\theta). \tag{22}$$

Dipolar (quadrupolar) magnetic fields have odd (even) values of ℓ in $a_\ell(r)$ and even (odd) values of ℓ in $b_\ell(r)$.

We compute the coefficients $a_\ell(r)$ and $b_\ell(r)$ from our simulations as

$$a_\ell(r) = N_\ell \int \overline{A}_\phi(r,\,\theta)\, P_\ell^1(\cos\theta)\, {\rm d}\cos\theta, \tag{23}$$

$$b_\ell(r) = N_\ell \int \overline{B}_\phi(r,\,\theta)\, P_\ell^1(\cos\theta)\, {\rm d}\cos\theta, \tag{24}$$

where $N_\ell = (2\ell + 1)\,(\ell - 1)!/(\ell + 1)!$ is a normalization factor. In particular, $N_1 = 3/2$ and $N_2 = 5/6$. In Figure 4, we plot the radial dependence of $a_{11}(r)$ and $b_{21}(r)$ for the dipolar case, and of $a_{21}(r)$ and $b_{11}(r)$ for the quadrupolar case. We clearly see the asymptotic slopes $a_{11} \propto r^{-2}$ and $b_{21} \propto r^{-3}$ for the dipole, and $b_{11} \propto r^{-2}$ and $a_{21} \propto r^{-3}$ for the quadrupole.

Note that for the dipolar and quadrupolar solutions, the roles of A_ϕ and B_ϕ are interchanged; see Figure 4. In particular, the r^{-2} behavior for the $\overline{A}_\phi$ of the dipole is now seen for the $\overline{B}_\phi$ field of the quadrupole, while the r^{-3} behavior for the $\overline{B}_\phi$ of the dipole is now seen for the $\overline{A}_\phi$ field of the quadrupole. Thus, although the poloidal component of a quadrupolar configuration still decays as r^{-4}, its toroidal component $\overline{B}_\phi$ decays as $\overline{A}_\phi$ for the dipolar configuration, i.e., as r^{-2}.

[10] In general, axisymmetric and nonaxisymmetric magnetic fields can be written as

$$\overline{\boldsymbol{B}} = \boldsymbol{\nabla}\times\boldsymbol{r}T + \boldsymbol{\nabla}\times\boldsymbol{\nabla}\times\boldsymbol{r}S, \tag{21}$$

where $T(r,\,\theta,\,\phi,\,t)$ and $S(r,\,\theta,\,\phi,\,t)$ are the superpotentials for the three-dimensional toroidal and poloidal fields, respectively. In axisymmetry, this implies that $B_\phi = -\,\partial T/\partial\theta$, and if $T(r,\,\theta) = P_\ell(\cos\theta)$, then $B_\phi = -P_\ell^1(\cos\theta)$. Likewise, using $A_\phi = -\,\partial S/\partial\theta$, and if $S(r,\,\theta) = P_\ell(\cos\theta)$, then $A_\phi = -P_\ell^1(\cos\theta)$.

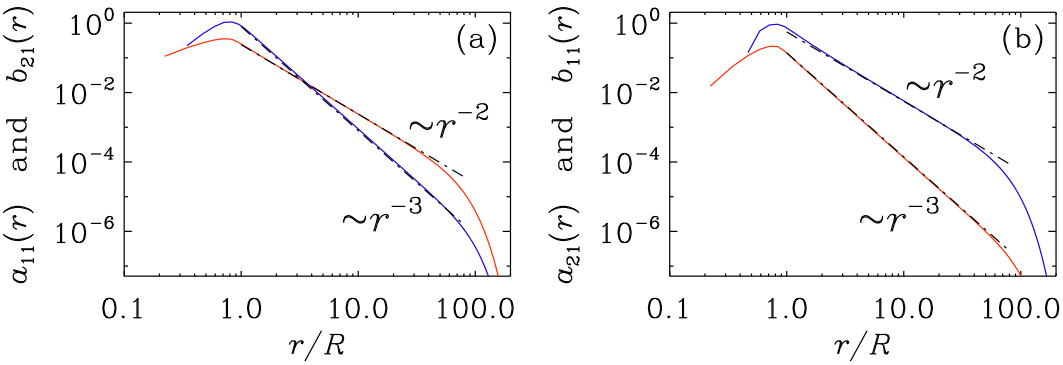

Figure 4. Radial dependence of (a) $a_{11}(r)$ and $b_{21}(r)$ for the dipolar case (Run A), and (b) $a_{21}(r)$ and $b_{11}(r)$ for the quadrupolar case (Run B). The asymptotic slopes are $a_{11}/(B_{\rm eq}R)\approx 0.052\ (r/R)^{-2}$ and $b_{21}/B_{\rm eq}\approx 0.3\ (r/R)^{-3}$ for the dipole, and $b_{11}/B_{\rm eq}\approx 0.132\ (r/R)^{-2}$ and $a_{21}/(B_{\rm eq}R)\approx 0.037\ (r/R)^{-3}$ for the quadrupole; these are marked with dashed–dotted lines. For a vacuum field, b_{11} would be zero. The red and blue lines indicate the scalings of $\overline{A}_\phi$ and $\overline{B}_\phi$, respectively, which are opposite for the dipolar and quadrupolar cases.

In the following, we discuss the individual components of the magnetic field in more detail. The two components of the poloidal field are given by $B_r = D_\theta A_\phi$ and $B_\theta = -D_r A_\phi$, where $D_\theta = r^{-1}\sin^{-1}\theta\,\partial_\theta(\sin\theta\ \cdot\ )$ and $D_r = r^{-1}\partial_r(r\ \cdot\ )$ are differential operators.

3.6. Lowest-order Dipole

Employing our lowest-order dipole approximation, we find the two fields to be proportional to

$$\bar{A}_\phi = a_D\, r^{-2}\, P_1^1(\cos\theta), \quad \bar{B}_\phi = b_D\, r^{-3}\, P_2^1(\cos\theta). \tag{25}$$

Therefore, since $P_1^1(\cos\theta) = -\sin\theta$ and $P_1(\cos\theta) = \cos\theta$, we have

$$\bar{B}_r = -2a_D\, r^{-3}\cos\theta \equiv -2a_D\, r^{-3}\, P_1(\cos\theta), \tag{26}$$

$$\bar{B}_\theta = -a_D\, r^{-3}\sin\theta \equiv a_D\, r^{-3}\, P_1^1(\cos\theta). \tag{27}$$

For our model, we find $a_D \approx 0.20\, B_{\rm eq}R^3$ and $b_{\rm D} \approx 0.60\, B_{\rm eq}R^3$.

3.7. Lowest-order Quadrupole

Our lowest-order quadrupole is proportional to

$$\overline{A}_\phi = a_{\rm Q}\, r^{-3}\, P_2^1(\cos\theta), \quad \overline{B}_\phi = b_{\rm Q}\, r^{-2}\, P_1^1(\cos\theta). \tag{28}$$

Since $P_2^1(\cos\theta) = -3\sin\theta\cos\theta$ and $P_2(\cos\theta) = (3\cos^2\theta - 1)/2$, we have

$$\overline{B}_r = 3a_{\rm Q}\, r^{-4}\,(1 - 3\cos^2\theta) \equiv -6a_{\rm Q}\, r^{-4}\, P_2(\cos\theta), \tag{29}$$

$$\overline{B}_\theta = -6a_{\rm Q}\, r^{-4}\sin\theta\cos\theta \equiv 2a_{\rm Q}\, r^{-4}\, P_2^1(\cos\theta). \tag{30}$$

For our model, we find $a_{\rm Q} \approx 0.09\, B_{\rm eq}R^4$ and $b_{\rm Q} \approx 0.49\, B_{\rm eq}R^2$.

3.8. Current Density Profiles

Next, we compute $\mu_0\overline{\boldsymbol{J}} = \boldsymbol{\nabla}\times\overline{\boldsymbol{B}}$, which is given by

$$\mu_0\overline{\boldsymbol{J}} = \hat{\boldsymbol{\phi}}\mu_0\overline{J}_\phi + \boldsymbol{\nabla}\times\hat{\boldsymbol{\phi}}\overline{B}_\phi, \tag{31}$$

where

$$\mu_0\bar{J}_\phi = -(D_r^2 + \mathcal{D}_\theta^2)\bar{A}_\phi \tag{32}$$

is proportional to the toroidal current density. Again, $D_r^2 \equiv D_r D_r$ and $\mathcal{D}_\theta^2 \equiv d_\theta D_\theta$, where $d_\theta = r^{-1}\partial_\theta$ is a convenient shorthand.

For the lowest-order dipole with $A_\phi = a_{\rm D}\, r^{-2}\, P_1^1(\cos\theta)$, we have

$$D_r^2(-r^{-2}\sin\theta) = -2\, r^{-4}\sin\theta \tag{33}$$

and

$$\mathcal{D}_\theta^2(-r^{-2}\sin\theta) = 2\, r^{-4}\sin\theta, \tag{34}$$

and therefore $\overline{J}_\phi = 0$. Thus, we have $\mu_0\overline{\boldsymbol{J}} = \boldsymbol{\nabla}\times\hat{\boldsymbol{\phi}}\overline{B}_\phi$, and the Lorentz force $\overline{\boldsymbol{J}}\times\overline{\boldsymbol{B}}$ is given by

$$\overline{\boldsymbol{J}}\times\overline{\boldsymbol{B}} = (\boldsymbol{\nabla}\times\hat{\boldsymbol{\phi}}\overline{B}_\phi)\times(\hat{\boldsymbol{\phi}}\overline{B}_\phi + \boldsymbol{\nabla}\times\hat{\boldsymbol{\phi}}\overline{A}_\phi)/\mu_0, \tag{35}$$

and has only a purely toroidal component whose divergence vanishes. Therefore, such a field is nearly force-free, except for the ϕ component, which drives only rotational motion. This agrees with our conclusion at the end of Section 3.2.

For the quadrupole with $\overline{A}_\phi \propto r^{-3}\sin\theta\cos\theta$, we have

$$D_r^2\, r^{-3} = 6\, r^{-5} \tag{36}$$

and

$$\mathcal{D}_\theta^2\sin\theta\cos\theta = -6\, r^{-2}\sin\theta\cos\theta. \tag{37}$$

Therefore, again $\overline{J}_\phi = 0$.

For the quadrupole, we have

$$D^2\overline{B}_\phi = 0, \tag{38}$$

in a manner similar to $\overline{A}_\phi$ for the dipolar field. However, unlike for $\overline{A}_\phi$, where $D^2\overline{B}_\phi = \mu_0\overline{J}_\phi$ is the toroidal current density, in the case of a quadrupolar field $D^2\overline{B}_\phi$ has no physically obvious meaning. What is more relevant in a conducting medium is the Lorentz force, $\overline{\boldsymbol{J}}\times\overline{\boldsymbol{B}}$, which has both poloidal and toroidal components. Its toroidal component, arising from the poloidal components $\overline{\boldsymbol{J}}_{\rm pol}$ and $\overline{\boldsymbol{B}}_{\rm pol}$, is nonvanishing, but it only drives azimuthal differential rotation and becomes extremely weak due to its rapid radial decay $\propto r^{-5}$. The poloidal Lorentz force has the components $\overline{\boldsymbol{J}}_{\rm pol}\times\overline{B}_\phi\hat{\boldsymbol{\phi}}$ and $\hat{\boldsymbol{\phi}}D^2\overline{A}_\phi \times \overline{\boldsymbol{B}}_{\rm pol}/\mu_0$fdoi. Using $\mu_0\overline{\boldsymbol{J}}_{\rm pol} = \boldsymbol{\nabla}\times\overline{B}_\phi\hat{\boldsymbol{\phi}}$ and $\overline{\boldsymbol{B}}_{\rm pol} = \boldsymbol{\nabla}\times\overline{A}_\phi\hat{\boldsymbol{\phi}}$, we have $(\boldsymbol{\nabla}\times\overline{B}_\phi\hat{\boldsymbol{\phi}})\times\overline{B}_\phi\hat{\boldsymbol{\phi}} = -\varpi^{-1}\boldsymbol{\nabla}(\varpi\overline{B}_\phi^2)$, which yields a radial force that also decays rapidly as r^{-5}. Thus, except for a term $\overline{B}_\phi^2\,\boldsymbol{\nabla}\ln\varpi^2$, the Lorentz force can in principle be balanced by a pressure gradient. The residual $\overline{B}_\phi^2\,\boldsymbol{\nabla}\ln\varpi^2$ term, on the

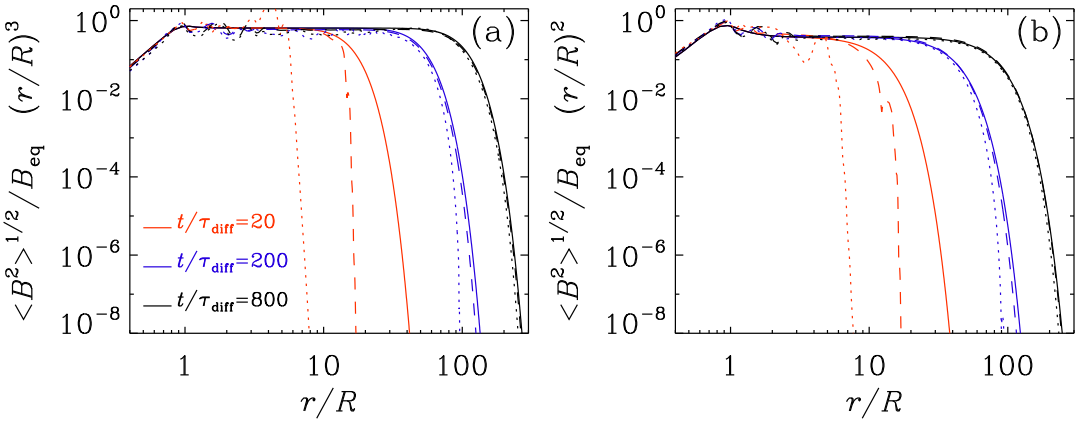

Figure 5. Radial magnetic field profiles compensated (a) by r^3 for the dipolar case (Runs D–F), and (b) by r^2 for the quadrupolar case (Runs G–I). For the solid lines, the displacement current is neglected (Runs D and G), while for the dashed and dotted lines it is included with $cR/\eta_{\rm eff}=1$ (Runs E and H) and 0.5 (Runs F and I), respectively. The red, blue, and black lines correspond to times $t/\tau_{\rm diff}=20$, 200, and 800.

other hand, can be balanced by the centrifugal force. In this sense, the quadrupolar configuration is nearly force-free.

As already stated above, outside the dynamo region $\overline{A}_\phi$ and $\overline{B}_\phi$ act independently of each other, and each component is subject to diffusion. Thus, unlike in the dynamo interior, where $\overline{B}_\phi$ is coupled to $\overline{A}_\phi$ through induction effects such as differential rotation, B_ϕ here expands purely through (turbulent) magnetic diffusion and can therefore adopt the same behavior as $\overline{A}_\phi$. In the present case, this means that for the quadrupolar configuration, $\overline{B}_\phi\propto r^{-2}$, just like the $\overline{A}_\phi\propto r^{-2}$ behavior for the dipolar configuration.

3.9. Effects of the Displacement Current

As seen from the Cartesian simulations in Appendix A, the inclusion of the displacement current can lead to a reduced growth rate γ; see Appendix A. It also can only decrease the front speed, $c_{\rm front}=\gamma/\kappa$. As a consequence, the front speed always remains below the speed of light.

As alluded to in Section 1, the magnetic diffusivity would need to be extremely large in order to emulate vacuum conditions. In vacuum, an electromagnetic wave propagates at the speed $c=300{,}000\,{\rm km\,s^{-1}}$, implying a propagation distance $L=ct_{\rm H}\approx5\,{\rm Gpc}$ in one Hubble time, $t_{\rm H}\approx14\,{\rm Gyr}$. This corresponds to a reference diffusivity of about $\eta_{\rm ref}\equiv L^2/t_{\rm H}=c^2t_{\rm H}\approx2\times10^{12}\,{\rm kpc\,km\,s^{-1}}$, which is nearly 10^9 times larger than the value $\eta_{\rm turb}=3000\,{\rm kpc\,km\,s^{-1}}$ used by O. Ghosh et al. (2026). Such large values are unrealistic.[11]

Nevertheless, it is of interest to see how the spherical expansion of the magnetic field is affected by the finite speed of light in a medium with such an extremely large effective magnetic diffusivity. In the following, we consider the values $cR/\eta_{\rm ref}=1$ and 0.5. Again, these ratios are chosen to be unrealistically small. This is done just to see the qualitative and quantitative effects of including the Faraday displacement current. We again choose $C_\eta=1$, which, as demonstrated above, does not affect the radial expansion compared to cases with larger values of C_η. The results for the spherical models are shown in Figure 5. For these models, we have neglected the evolution of the mean flow, i.e., we solve only Equations (5) and (6). We find that only at early times is the solution noticeably affected by the finite speed of light—even for $cR/\eta_{\rm eff}=0.5$. In these cases, as explained in Section 2.2, we characterize the front radius by the radius $r_{0.01}$, where the compensated magnetic field has dropped to 0.01 times its value inside the magnetosphere. From Table 1, we see that $r_{0.01}/ct<1$ is satisfied in all cases with finite values of $cR/\eta_{\rm eff}$. This ratio varies between 0.8 and 0.6 for our dipolar configurations (Runs E and F) and between 0.7 and 0.6 (Runs H and I) for our quadrupolar configurations. Thus, $r_{0.01}$ remains close to, but always below, the Hubble radius.

3.10. Effects of Changing r_{in} and h

In Figure 6, we examine the effects of varying the ratios $r_{\rm in}/R$ and h/R (Runs J–L). To ensure that the dynamo remains excited despite its smaller volume, we have here also increased the value of C_α from 25 to 50. We find that the radial falloff is basically unchanged when increasing the value of $r_{\rm in}/R$ from 0.1 (Run G) to 0.2 (Run J). By contrast, decreasing the value of h/R from 1 (Run G) to 0.5 (Run K) and 0.2 (Run L) leads to more complex radial profiles, including the development of radial oscillations. In addition, there is an indication of a reduction in the magnetic field strength in the wake of the front. To examine this more clearly, we run the case with $h/R=0.2$ for a much longer time. The results suggest that the magnetic field forms an azimuthal ring, or at least a shell, rather than a filled sphere. This complication obscures the otherwise simple radial power-law behavior discussed above, and also motivates our focus on the case $H/R=1$. It is important to note, however, that the position of the exponential falloff at the edge of the magnetosphere remains unchanged, as evidenced by the nearly constant value of the parameter $q_{\rm diff}$ listed in Table 1 and by the fits presented in Figure 6 for the final time step.

4. Observational Implications

To compare with future observations, O. Ghosh et al. (2026) computed the rotation measure (RM). Assuming a radial power-law dependence for the thermal electron density, $n_{\rm th}\propto r^{-s_{\rm th}}$, they found that RM decreases with radius as $r^{-2-s_{\rm th}}$ for the dipolar solution and as $r^{-1-s_{\rm th}}$ for the quadrupolar solution. Measuring such radial profiles can therefore help to test our predicted scalings.

[11] Even if the turbulent velocity were equal to the speed of light, it would require a correlation length of more than 70 Gpc to reach a turbulent diffusivity of 10^{12} kpc km s^{-1}.

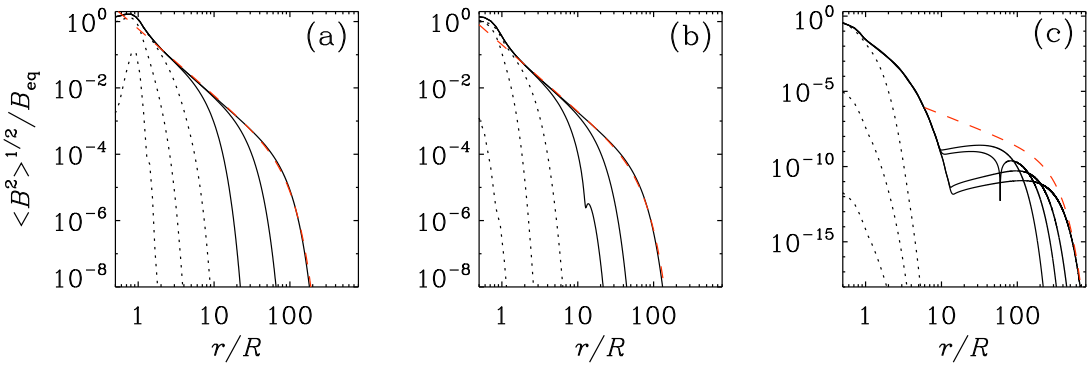

Figure 6. Radial magnetic field profiles for Runs J, K, and L. For Run J, we have $r_{\rm in}/R = 0.2$ instead of 0.1, while for Runs K and L, we have $h/R = 0.5$ and 0.2, respectively. The times are (a) $t/\tau_{\rm diff} = 0.1$, 0.3, and 1.5 for the dotted lines, and 10, 100, and 942 for the solid lines; (b) 0.1, 0.2, and 0.8 for the dotted lines, and 10, 50, and 530 for the solid lines; and (c) 0.2, 0.4, and 0.6 for the dotted lines, and 500, 1200, 2700, and 5990 for the solid lines.

Another observational diagnostic is the resulting synchrotron emission. The synchrotron intensity $I(x, z, \lambda)$ and the complex polarization $\mathcal{P}(x, z, \lambda) \equiv Q + {\rm i}U$ are obtained by line-of-sight integration. Here, Q and U are the Stokes parameters characterizing linear polarization, and λ is the wavelength.

To illustrate the basic properties of I, Q, and U, we adapt the expression for the radial scaling of the magnetic field given by Equation (17) to the lowest-order dipolar and quadrupolar configurations discussed in Sections 3.6 and 3.7. We then compute the components

$$\overline{B}_x = \sin\theta\cos\phi\,\overline{B}_r + \cos\theta\cos\phi\,\overline{B}_\theta - \sin\phi\,\overline{B}_\phi, \quad (39)$$

$$\overline{B}_z = \cos\theta\,\overline{B}_r - \sin\theta\,\overline{B}_\theta, \quad (40)$$

in Cartesian coordinates, where ϕ is the azimuthal angle and θ is the colatitude. The synchrotron intensity $I(x, z)$ projected onto the x–z plane is given by

$$I(x, z, \lambda) = \int_{-L}^{L} \epsilon(x, y', z, \lambda)\,{\rm d}y', \quad (41)$$

where $\epsilon \propto n_{\rm CR}\overline{B}_\perp^{(\varsigma+1)/2}\lambda^{(\varsigma-1)/2}$ is the emissivity, $n_{\rm CR}$ is the cosmic-ray density, λ is the wavelength, and ς is the spectral index of the momentum distribution (V. L. Ginzburg & S. I. Syrovatskii 1965). Realistic values for ς lie in the range 2.8–3.2, as a result of the combination of continuous injection of secondary electrons (by hadronic collisions), injection of primary electrons by supernova-driven shocks, and modulation by energy-dependent diffusion (e.g., R. Beck 1991; M. Werhahn et al. 2021; L. Armillotta et al. 2025). Here, for simplicity, we use $\varsigma = 3$, in which case $\epsilon \propto \overline{B}_\perp^2$, and the complex intrinsic polarization is simply proportional to $\mathcal{B}_\perp^2$, where $\mathcal{B}_\perp = \overline{B}_x + {\rm i}\overline{B}_z$ is the complex magnetic field in the plane of the sky; see A. Brandenburg & R. Stepanov (2014) for earlier work utilizing this formalism.

We neglect the effects of Faraday rotation, which would introduce a factor $\exp(2{\rm i}\phi\lambda^2)$ under the integral of $\mathcal{P}$. This is justified by the results of O. Ghosh et al. (2026), who showed that Faraday rotation is negligible outside the galactic core. Here, $\phi(x, y, z) = -K\int_0^y (n_{\rm th}\overline{B}_y)(x, y', z)\,{\rm d}y'$ is the Faraday depth and K is a known constant. Neglecting Faraday rotation corresponds to taking the limit $\lambda \to 0$.

In Figure 7, we present synthetic maps of the synchrotron intensity $I(x, z)$ for the same dipolar and quadrupolar configurations as in O. Ghosh et al. (2026), corresponding to Runs A and B, respectively. For $n_{\rm CR}$, we assume for simplicity a steady radial profile similar to $n_{\rm th}$, which we write as $n_{\rm CR} \propto r^{-s_{\rm CR}}$, analogous to the expression used for $n_{\rm th}$ by O. Ghosh et al. (2026). Here, we adopt $s_{\rm CR} = 1$, although it should be noted that radiative losses may complicate this behavior in reality (e.g., G. Peron et al. 2021; C. Pfrommer et al. 2022; L. Armillotta et al. 2025). To obtain a quantitative estimate of the magnetospheric emission, we use (G. B. Rybicki & A. P. Lightman 1986; see also Appendix C)

$$\epsilon\,{\rm d}y \approx \frac{5\,\mu{\rm Jy}}{\rm sr}\left(\frac{n_{\rm CR}^{(100\,{\rm kpc})}}{10^{-7}\,{\rm cm}^{-3}}\right)\left(\frac{B_{\rm eq}}{1\,\mu{\rm G}}\right)^2\left(\frac{\lambda}{2\,{\rm m}}\right)\left(\frac{{\rm d}y}{1\,{\rm kpc}}\right), \quad (42)$$

where $n_{\rm CR}^{(100\,{\rm kpc})}$ is the cosmic-ray density at a galactocentric distance of 100 kpc, assuming that $s_{\rm CR} = 1$ remains valid at that distance, which in turn depends on the long-term integrated dispersal of cosmic rays around galaxies and within large-scale structures (see, e.g., F. Vazza et al. 2025 for recent numerical studies).

In Figure 7, we overlay the polarization vectors (Q, U). For a power-law dependence of the cosmic-ray number density, $n_{\rm CR} \propto r^{-s_{\rm CR}}$, assuming $\overline{B}_\perp \propto r^{-n}$ with $n = 2$ for quadrupoles and $n = 3$ for dipoles, the intrinsic emissivity becomes proportional to $n_{\rm CR}\overline{B}_\perp^2 \propto r^{-s_{\rm CR}-2n}$; see Equation (17). Line-of-sight integration adds another power, yielding $r^{-s_{\rm CR}-2n+1}$. Thus, for quadrupolar (dipolar) configurations, we find $I \propto r^{-3-s_{\rm CR}}$ ($\propto r^{-5-s_{\rm CR}}$).

We find that the polarization vectors are predominantly in the x-direction. This is a commonly observed feature related to the dominance of the toroidal magnetic field; see, e.g., A. Brandenburg et al. (1993) and D. Elstner et al. (1995) for earlier work where, unlike the present case, a radial wind was included. Only in the dipolar configuration does the toroidal field change sign at the midplane, leading to clear deviations from the otherwise nearly perfect alignment of the polarization vectors with the x-direction.

As expected, the radial falloff of the synchrotron intensity is still rather steep—even for the quadrupolar configuration. Let us therefore now discuss whether our predicted intensity distributions are observable in real galaxies. For example, an 8 hr integration with the LOFAR High Band Antenna at ≈150 MHz typically reaches a noise level of $3\sigma_{\rm rms} \approx 1\,\mu{\rm Jy\,arcsec}^{-2} = 2.35\cdot10^{-17}\,{\rm Jy\,sr}^{-1}$. Based on Figure 7, a fraction of the predicted radio emission should be detectable in both cases by radio telescopes. However, for the dipolar configuration, the detectable region is likely confined within a ⩽200 kpc radius, whereas for the quadrupolar case a

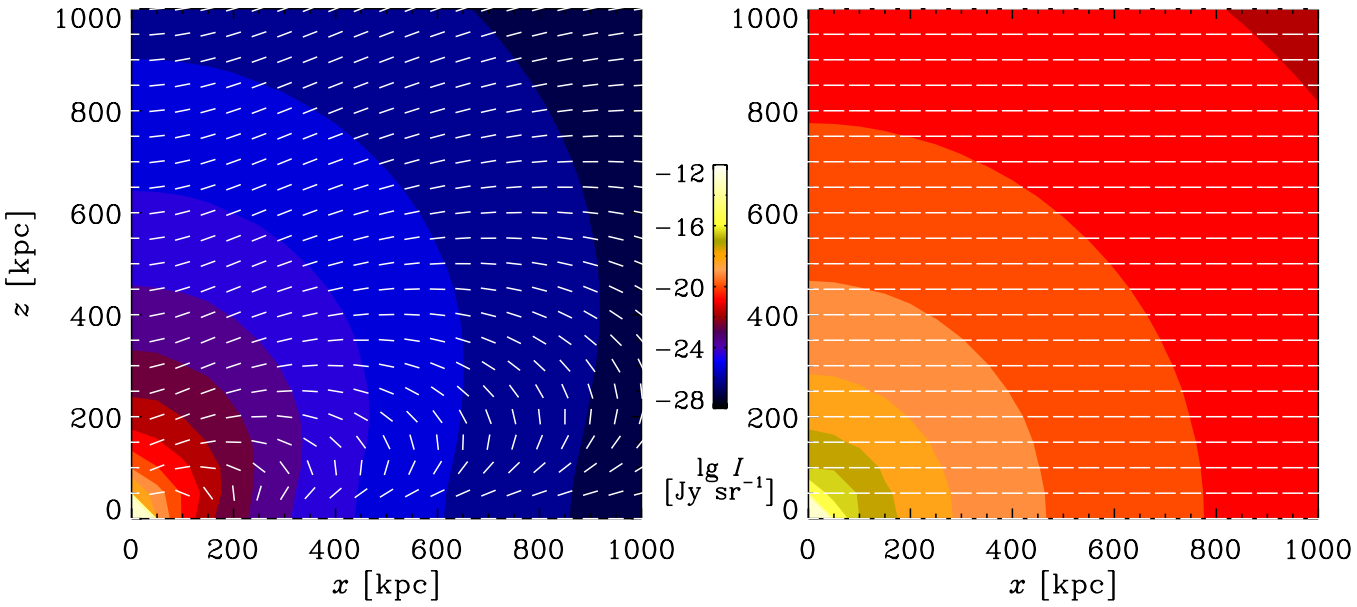

Figure 7. Polarization vectors (Q, U) superimposed on a color-scale representation of the logarithmic intensity $I(x, z)$ (in Jy sr^{-1}) for Runs A (dipolar configuration, left) and B (quadrupolar configuration, right).

much larger region may be detectable. A quantitative prediction requires fixing the radial distribution of cosmic rays, which can currently only be guessed at. In real galaxies, this distribution is likely affected by the presence of large-scale outflows, especially at larger radii where the inertia of cosmic rays is expected to become dynamically dominant (e.g., H. H. S. Chiu et al. 2024). Interestingly, however, the orientation of the polarization vectors is relatively insensitive to the distribution of relativistic electrons. This is unfortunate, because the orientation of the polarization vectors could provide a more direct probe of the large-scale distribution of magnetic fields. Intriguingly, preliminary work using LOFAR observations may already have yielded results that are consistent with our prediction of a finite magnetosphere (M. S. S. L. Oei 2025, private communication).

Distinguishing whether the magnetosphere is produced by a galactic wind or by turbulent magnetic diffusion is not straightforward, as both mechanisms lead to the same r^{-2} flux-conserving radial decay. However, combined spectral and polarimetric observations at large radii have been shown to provide a sensitive diagnostic of cosmic-ray (re)acceleration processes (e.g., S. Taziaux et al. 2025). Such cosmic rays are expected in the presence of outflows (e.g., H. H. S. Chiu et al. 2024), but not necessarily in the case of the extended magnetosphere studied in this work.

5. Conclusions

We have studied the radial spreading of a dynamo-generated magnetic field into its electrically conducting surroundings. Unlike in conventional dynamo theory, where the exterior field is assumed to be a current-free potential field, our solution contains electric currents and is only approximately force-free. As already reported by O. Ghosh et al. (2026), the quadrupolar field has a toroidal component that decays with radius as r^{-2}, which is slower than the r^{-3} decay of the dipolar poloidal component in the far field of the dynamo. To the best of our knowledge, such a slow radial decay has not been reported previously.

An important difference from earlier work on force-free magnetic fields in dynamo exteriors is that we study the time-dependent case using direct numerical simulations, in which a nearly force-free field builds up gradually in an electrically conducting medium. As far as the formulation of effective boundary conditions is concerned, which was the main purpose of considering force-free exteriors (A. Bonanno 2016; A. Bonanno & F. Del Sordo 2017), the finite time required to establish the exterior field may not be critical on such short length scales. However, the slower radial decay and the sharp exponential falloff marking the edge of the magnetosphere may be of observational interest (O. Ghosh et al. 2026) and could be tested with the new generation of radio observatories (e.g., M. Ghasemi-Nodehi et al. 2022). This feature may help distinguish such fields from dipolar configurations on the one hand and from wind-governed ones on the other. Galactic winds have indeed frequently been studied in simulations (A. Aramburo-García et al. 2021, 2022; K. Bondarenko et al. 2022), including cases in which a dynamo is coupled either to an imposed wind (A. Brandenburg et al. 1993) or to a dynamically sustained one (P. Jakab & A. Brandenburg 2021; B. Perri et al. 2021).

In the work of A. Brandenburg et al. (1993), maps of synchrotron emission were presented, but the displayed results do not allow a clear determination of whether the radial falloff is characterized by a power law. P. Jakab & A. Brandenburg (2021) did not compute synchrotron emission, but they presented their results for $\overline{B}_\phi$ compensated by r^2. This shows that, although their field configuration was dipolar, the presence of a wind alone can lead to a slow radial decay of $\overline{B}_\phi$.

In the present cases, an important clue to understanding the origin of the r^{-2} decay of $\overline{B}_\phi$ comes from the correspondence between the $(\overline{B}_\phi, \overline{A}_\phi)$ pair for a quadrupolar configuration and the $(\overline{A}_\phi, \overline{B}_\phi)$ pair for a dipolar configuration. In both cases, the residual components decay as

$$\left.\begin{matrix}(\overline{B}_\phi, \overline{A}_\phi)\\ (\overline{A}_\phi, \overline{B}_\phi)\end{matrix}\right\} = [r^{-2}\ \ P_1^1(\cos\theta),\ \ r^{-3}\ \ P_2^1(\cos\theta)], \tag{43}$$

and their evolution is simply the result of diffusion. Unlike the α- and Ω-effects in the dynamo interior, diffusion does not couple $\overline{A}_\phi$ and $\overline{B}_\phi$, which makes this correspondence possible.

While these results are also borne out in cases where the displacement current is included, we have shown that it can safely be ignored in all cases of interest. Its main role lies in limiting the expansion speed in poorly conducting media rather than facilitating a radial expansion.

It is also interesting to note that the far-field magnetic field configurations are nearly force-free, in the sense that the resulting Lorentz force can be balanced by pressure-gradient and centrifugal forces. However, this aspect is likely subdominant, as the Lorentz force decays rapidly with radius and our results are essentially independent of whether the momentum equation is included.

In the present work, we have made a number of simplifying assumptions that have helped produce clean results. In particular, assuming a spherical rather than an oblate dynamo geometry helps produce a power-law behavior in the radial decay of the magnetic field. It is possible that, at large distances from the dynamo region, this assumption becomes less critical. However, the present results for oblate dynamo geometries suggest that the magnetosphere may instead take the form of a ring or a spherical shell. The inclusion of differential rotation in the dynamo region would further complicate the results. Preliminary studies have shown that the r^{-2} falloff for the quadrupolar configuration may become steeper. It remains unclear, however, how this changes at larger distances. Further modifications are expected if a radial wind is allowed to develop. In that case, the results may depend on the level of galactic activity driving such a wind. Nevertheless, a slow radial falloff for quadrupolar fields may still survive under certain more realistic conditions. As explained above, the resulting synchrotron emission may be of observational interest. However, as already stressed by O. Ghosh et al. (2026), the radii of galactic magnetospheres are not affected by this and remain prohibitively small in view of scenarios, such as that proposed by D. Garg et al. (2025), in which the lower limits of void magnetization are explained by the superposition of dipoles from the far field of galaxies.

Acknowledgments

We thank the referee for a constructive review. We acknowledge stimulating discussions with Ruth Durrer, Deepen Garg, and Jennifer Schober. This research was supported in part by the European Research Council through the ERC Synergy Grant COSMOMAG under grant No. 101224803, the Swedish Research Council (Vetenskapsrådet) under grant No. 2025-05957, the National Science Foundation under grant Nos. NSF AST-2307698 and AST-2408411, and NASA Award No. 80NSSC22K0825. O.G. acknowledges support from a Wallenberg Academy Fellowship (PI: Azadeh Fattahi). Additionally, O.G. is supported by the Swedish Research Council (Vetenskapsrådet) under contracts 2022-04283 and 2019-02337 and additionally by the Göran Gustafsson Foundation for Research in Natural Sciences and Medicine. A.N. is partially supported by the French National Research Agency (ANR) grant No. ANR-24-CE31-4686. F.V. has been partially supported by Fondazione Cariplo and Fondazione CDP, through grant No. Rif: 2022-2088 CUP J33C22004310003 for the "BREAKTHRU" project. We acknowledge the allocation of computing resources provided by the Swedish National Allocations Committee at the Center for Parallel Computers at the Royal Institute of Technology in Stockholm.

Software and Data Availability. The source code used for the simulations of this study, the PENCIL CODE (Pencil Code Collaboration et al. 2021), is freely available on https://github.com/pencil-code. The simulation setups and corresponding input and reduced output data are freely available on doi:10.5281/zenodo.18564321.

Appendix A
Dispersion Relation for a Dynamo with Constant Coefficients

To illuminate the mean-field dynamo behavior for a finite speed of light and to provide a benchmark for testing purposes, we discuss here the case of an α^2 dynamo with constant coefficients. Seeking solutions proportional to $\exp(\gamma t + \mathrm{i}\boldsymbol{k}\cdot\boldsymbol{x})$, the dispersion relation $\gamma(\boldsymbol{k})$ can be obtained by solving for the roots of

$$\left[\gamma + \eta_{\rm eff}k^2\left(1 + \frac{\gamma^2}{c^2k^2}\right)\right]^2 - \alpha^2k^2 = 0. \tag{A1}$$

In the limit $c \to \infty$, the dispersion relation agrees with the conventional one:

$$\gamma = \pm|\alpha|k - \eta_{\rm eff}k^2. \tag{A2}$$

Figure 8 shows $\gamma(\alpha)$ for a fixed value of $k = k_1$ and three values of $c/\eta_{\rm eff}k_1$. The dependence matches the conventional one for $c \to \infty$. We see that the effect of a finite speed of light is to lower the value of γ.

For $\alpha = 0$, the growth rate is always negative. There are then two branches, given by

$$\gamma_\pm = -[1 \pm \sqrt{1 - (2\eta_{\rm eff}k/c)^2}\,]\,c^2/2\eta_{\rm eff}. \tag{A3}$$

For $k > c/2\eta_{\rm eff}$, i.e., for $k/k_1 > c/2\eta_{\rm eff}k_1$, γ is complex, i.e., the solutions are oscillatory with the growth rate $\mathrm{Re}\gamma = -c^2/2\eta_{\rm eff}$, which is independent of k. This is shown in Figure 9, where we plot the negative normalized growth rate versus k/k_1 for different values of $c/\eta_{\rm eff}k_1$. Evidently, only for $c/\eta_{\rm eff}k_1 > 2$ are the solutions nonoscillatory for all wavenumbers.

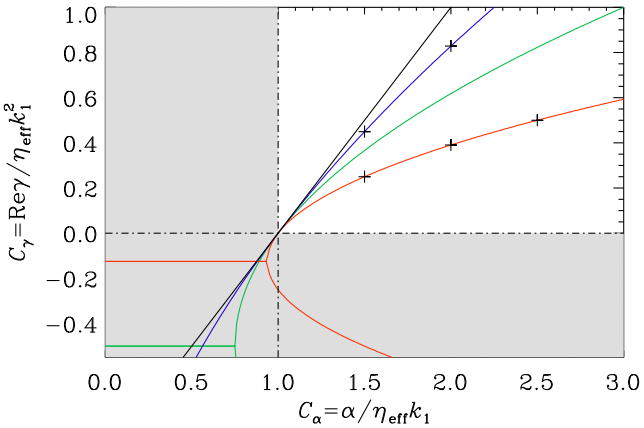

Figure 8. Growth rate vs. dynamo number $\alpha/\eta_{\rm eff}k_1$ for a fixed value of $k = k_1$ and $c/\eta_{\rm eff}k = 0.5$ (red), 1 (green), and 2 (blue). The gray areas mark the regions of no growth. The conventional dependence for $c \to \infty$ corresponds to the black line. The black plus signs refer to data points obtained using the PENCIL CODE.

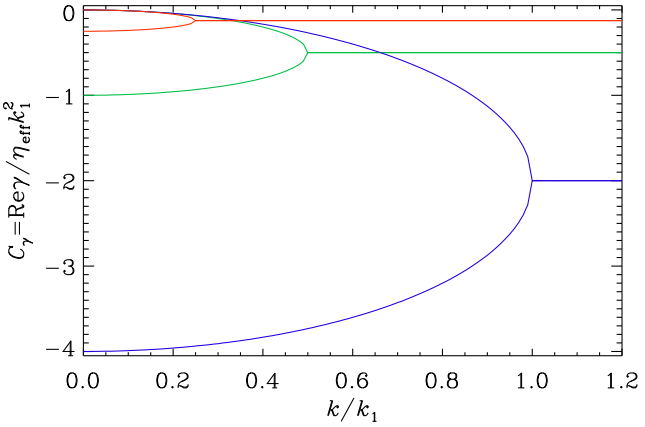

Figure 9. Normalized growth rate vs. k/k_1 for $\alpha = 0$ and $c/\eta_{\rm eff}k_1 = 0.5$ (red), 1 (green), and 2 (blue). For $k > c/2\eta_{\rm eff}$, the two solutions are oscillatory with a complex conjugated pair of eigenvalues whose real part is independent of k.

For an exponentially growing magnetic field, the spatial spreading can be described by $\overline{\boldsymbol{B}} \propto e^{-\kappa(z-c_{\rm front}t)}$, where $c_{\rm front}$ is the front speed, $\kappa c_{\rm front} = \gamma$ is the growth rate, and $\kappa = k$. This relation is only valid outside the dynamo-active region, where $\alpha = 0$. Since the effect of a finite speed of light is to lower the value of γ, this also lowers the front speed γ/k. For the conventional dispersion relation, the front speed is given by

$$c_{\rm front} = \gamma/k = |\alpha| - \eta_{\rm eff}k. \tag{A4}$$

For finite values of c, the front speed is lowered, except for the marginal point when k exceeds the critical value below which dynamo action is possible. This is shown in Figure 10 for three finite values of $c/\eta_{\rm eff}k$. We see that the line for $c/\eta_{\rm eff}k = 2$ is already rather close to the case $c \to \infty$. As discussed in the bulk of the present paper, $c/\eta_{\rm eff}k$ is indeed very large for realistic values of ηT and k. Therefore, the Faraday displacement current can indeed be neglected for all practical purposes.

As expected, the front speed never exceeds the speed of light. By contrast, however, the input parameters α and $\eta_{\rm eff}k$, which also have the dimensions of a speed, can exceed c. Whether such values can be physically realized is, however, open to question.

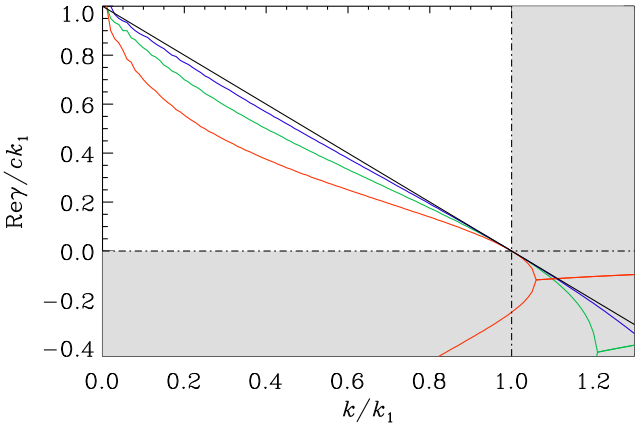

Figure 10. Front speed γ/k (in units of c) vs. k (in units of $c/\eta_{\rm eff}$) for $\alpha/c = 1$ and $c/\eta_{\rm eff}k = 0.5$ (red), 1 (green), and 2 (blue). As in Figure 8, the gray areas mark the regions of no growth. The conventional line for $c \to \infty$ corresponds to the black line.

Appendix B
Power-law Growth of ηT

For the quadrupolar case, the inverse-quadratic radial falloff is still approximately obeyed even when $\eta_{\rm eff}$ is not constant for $r > R$. This is demonstrated in Figure 11, where we compare the mean radial magnetic field profiles for Runs G, G′, and G″. The slopes do not depart markedly from the r^{-2} decay. For a more quantitative demonstration, we also show, for Runs G′ and G″, the profiles compensated by r^{+n} with $n = 2.16$ and $n = 2.23$, respectively. This confirms that the decay exponents given in Table 1 are accurately determined.

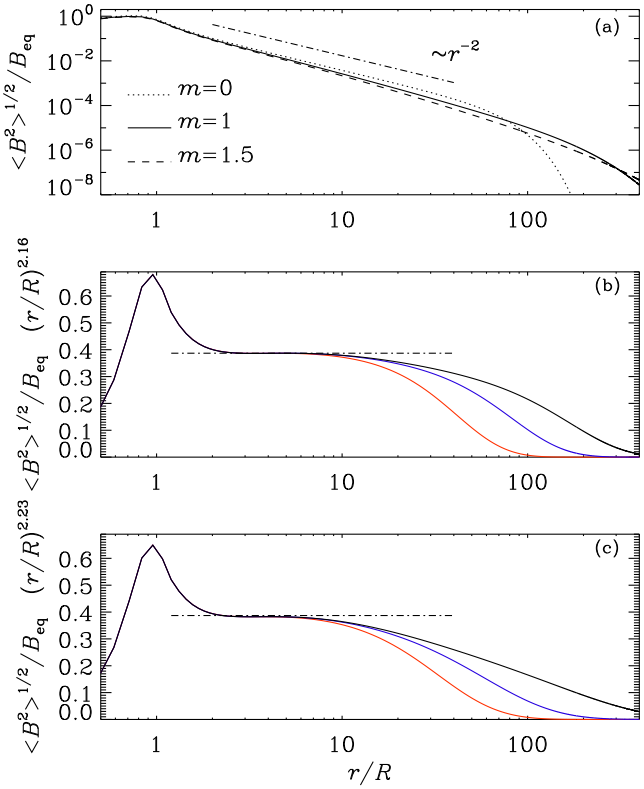

Figure 11. (a) Radial magnetic field profiles for the quadrupolar Runs G, G′, and G″. Runs G′ and G″ have a radially increasing $\eta_{\rm eff}(r)$ profile. In panels (b) and (c), the mean magnetic field profiles are compensated by $r^{2.16}$ and $r^{2.23}$, respectively. The red, blue, and black lines correspond to times $t/\tau_{\rm diff} = 100$, 250, and 600 for Run G′, and $t/\tau_{\rm diff} = 50$, 100, and 250 for Run G″.

Appendix C
Derivation of Equation (41)

The purpose of this appendix is to provide the detailed derivation of Equation (42). Following G. B. Rybicki & A. P. Lightman (1986), we consider a power-law distribution of cosmic rays such as $N(E)dE = CE^{-\varsigma}dE, \quad E_{\rm min} < E < E_{\rm max}$ with a particle distribution index ς corresponding to a spectral index s given by $s = (\varsigma - 1)/2$, such that $P_{\rm tot}(\omega) \propto \omega^{-(\varsigma-1)/2}$. The normalization can be determined from the cosmic-ray number density,

$$n_{\rm CR} = C\frac{E_{\rm max}^{1-\varsigma} - E_{\rm min}^{1-\varsigma}}{1-\varsigma}, \tag{C1}$$

for $E_{\rm min} < E < E_{\rm max}$, known as the band-limited case. However, if $E_{\rm max} \to \infty$, normalization C depends only on

the threshold energy $E_{\rm min}$ for $\varsigma > 1$ as

$$C = n_{\rm CR}(\varsigma - 1)E_{\rm min}^{\varsigma-1}. \quad \text{(C2)}$$

The total synchrotron power per unit volume per unit frequency irradiated by such a population of cosmic rays can be written as

$$P_{\rm tot}(\nu) = \frac{\sqrt{3}\ q^3 {\rm C}\, B \sin\alpha}{mc^2(\varsigma+1)}\, C_2 \left(\frac{2\pi mc\nu}{3qB\sin\alpha}\right)^{\frac{1-\varsigma}{2}}, \quad \text{(C3)}$$

Based on this, the optically thick surface brightness can be expressed in general as

$$I_\nu \propto n_{CR}(>E_{\rm min})E_{\rm min}^{\varsigma-1}B^{(1+\varsigma)/2}L\nu^{(1-\varsigma)/2}. \quad \text{(C4)}$$

Taking the equipartition magnetic field $B = B_{\rm eq}$, averaging over the pitch-angle factor $\langle \sin^{(1+\varsigma)/2}\alpha\rangle$, and finally setting the index $\varsigma = 3$, we obtain an optically thick surface brightness of the form

$$I_\nu \approx 5 \times 10^{-6}\,{\rm Jy\ sr^{-1}} \left(\frac{n_{\rm CR}}{10^{-7}\,{\rm cm^{-3}}}\right)\left(\frac{E_{\rm min}}{100\,{\rm MeV}}\right)^2 \times \left(\frac{B}{1\,\mu{\rm G}}\right)^2\left(\frac{L}{1\,{\rm kpc}}\right)\left(\frac{\nu}{150\,{\rm MHz}}\right)^{-1}. \quad \text{(C5)}$$

Replacing $(\nu/150\,{\rm MHz})^{-1}$ with $(\lambda/2\,{\rm m})$ and using $E_{\rm min} = 100$ MeV, we arrive at Equation (42).

ORCID iDs

Axel Brandenburg https://orcid.org/0000-0002-7304-021X
Oindrila Ghosh https://orcid.org/0000-0003-2226-0025
Franco Vazza https://orcid.org/0000-0002-2821-7928
Andrii Neronov https://orcid.org/0000-0002-6748-368X

References

Aramburo-García, A., et al. 2021, MNRAS, 502, 6012
Aramburo-García, A., et al. 2022, MNRAS, 514, 2656
Armillotta, L., Ostriker, E. C., & Linzer, N. B. 2025, ApJ, 989, 140
Beck, R. 1991, A&A, 251, 15
Bonanno, A. 2016, ApJL, 833, L22
Bonanno, A., & Del Sordo, F. 2017, A&A, 605, A33
Bondarenko, K., Boyarsky, A., Korochkin, A., et al. 2022, A&A, 660, A80
Brandenburg, A., Donner, K. J., Moss, D., et al. 1993, A&A, 271, 36
Brandenburg, A., Haugen, N. E. L., & Babkovskaia, N. 2011, PhRvE, 83, 016304
Brandenburg, A., Moss, D., & Tuominen, I. 1992, A&A, 265, 328
Brandenburg, A., & Stepanov, R. 2014, ApJ, 786, 91
Brandenburg, A., Tuominen, I., & Krause, F. 1990, GApFD, 50, 95
Chandrasekhar, S., & Kendall, P. C. 1957, ApJ, 126, 457
Chiu, H. H. S., Ruszkowski, M., Thomas, T., Werhahn, M., & Pfrommer, C. 2024, ApJ, 976, 136
Einstein, A. 1905, AnP, 322, 549
Elstner, D., Golla, G., Rüdiger, G., & Wielebinski, R. 1995, A&A, 297, 77
Elstner, D., Meinel, R., & Rüdiger, G. 1990, GApFD, 50, 85
Freidberg, J. P. 2014, Ideal MHD (Cambridge Univ. Press)
Garg, D., Durrer, R., & Schober, J. 2025, arXiv:2505.14774
Ghasemi-Nodehi, M., Tabatabaei, F. S., Sargent, M., et al. 2022, MNRAS, 515, 1158
Ghosh, O., Brandenburg, A., Caprini, C., Neronov, A., & Vazza, F. 2026, PhRvD, 113, 023523
Ginzburg, V. L., & Syrovatskii, S. I. 1965, ARA&A, 3, 297
Ivanova, T. S., & Ruzmaikin, A. A. 1977, SvA, 21, 479
Jabbari, S., Brandenburg, A., Kleeorin, N., Mitra, D., & Rogachevskii, I. 2015, ApJ, 805, 166
Jakab, P., & Brandenburg, A. 2021, A&A, 647, A18
Kitchatinov, L. L., & Rüdiger, G. 1995, A&A, 299, 446
Krause, F., & Rädler, K.-H. 1980, Mean-Field Magnetohydrodynamics and Dynamo Theory (Pergamon Press)
Meinel, R., Elstner, D., & Ruediger, G. 1990, A&A, 236, L33
Moffatt, H. K. 1978, Magnetic Field Generation in Electrically Conducting Fluids (Cambridge Univ. Press)
Murray, J. D., Stanley, E. A., & Brown, D. L. 1986, RSPSB, 229, 111
Parker, E. N. 1979, Cosmical Magnetic Fields: Their Origin and Their Activity (Clarendon Press)
Pencil Code Collaboration, Brandenburg, A., Johansen, A., et al. 2021, JOSS, 6, 2807
Peron, G., Aharonian, F., Casanova, S., Yang, R., & Zanin, R. 2021, ApJL, 907, L11
Perri, B., Brun, A. S., Strugarek, A., & Réville, V. 2021, ApJ, 910, 50
Pfrommer, C., Werhahn, M., Pakmor, R., Girichidis, P., & Simpson, C. M. 2022, MNRAS, 515, 4229
Priest, E. R. 1982, Solar Magnetohydrodynamics, Vol. 21 (D. Reidel)
Rempel, M. 2006, ApJ, 647, 662
Rybicki, G. B., & Lightman, A. P. 1986, Radiative Processes in Astrophysics (Wiley-VCH)
Schüssler, M. 1979, A&A, 72, 348
Seller, K., & Sigl, G. 2025, arXiv:2510.08025
Steenbeck, M., & Krause, F. 1969, AN, 291, 49
Stix, M. 1975, A&A, 42, 85
Taziaux, S., Müller, A., Adebahr, B., et al. 2025, A&A, 696, A226
Vazza, F., Gheller, C., Zanetti, F., et al. 2025, A&A, 696, A58
Werhahn, M., Pfrommer, C., Girichidis, P., Puchwein, E., & Pakmor, R. 2021, MNRAS, 505, 3273
Yang, W. H., Sturrock, P. A., & Antiochos, S. K. 1986, ApJ, 309, 383